

RESEARCH ARTICLE

10.1002/2014JF003246

Evolution of Derwael Ice Rise in Dronning Maud Land, Antarctica, over the last millennia

R. Drews¹, K. Matsuoka², C. Martín³, D. Callens¹, N. Bergeot⁴, and F. Pattyn¹¹Laboratoire de Glaciologie, Université Libre de Bruxelles, Brussels, Belgium, ²Norwegian Polar Institute, Tromsø, Norway, ³British Antarctic Survey, Cambridge, UK, ⁴Observatoire Royal de Belgique, Brussels, Belgium

Key Points:

- Derwael Ice Rise has maintained a local flow regime over thousands of years
- Arches in ice stratigraphy are explicable with anisotropic rheology and thinning
- Surface mass balance at the divide is important for modeling ice-rise evolution

Correspondence to:

R. Drews,
rdrews@ulb.ac.be

Citation:

Drews, R., K. Matsuoka, C. Martín, D. Callens, N. Bergeot, and F. Pattyn (2015), Evolution of Derwael Ice Rise in Dronning Maud Land, Antarctica, over the last millennia, *J. Geophys. Res. Earth Surf.*, 120, 564–579, doi:10.1002/2014JF003246.

Received 12 JUN 2014

Accepted 19 FEB 2015

Accepted article online 24 FEB 2015

Published online 20 MAR 2015

Abstract Ice rises situated in the ice-shelf belt around Antarctica have a spatially confined flow regime with local ice divides. Beneath the divides, ice stratigraphy often develops arches with amplitudes that record the divide's horizontal residence time and surface elevation changes. To investigate the evolution of Derwael Ice Rise, Dronning Maud Land, Antarctica, we combine radar and GPS data from three consecutive surveys, with a two-dimensional, full Stokes, thermomechanically coupled, transient ice-flow model. We find that the surface mass balance (SMB) is higher on the upwind and lower on the downwind slopes. Near the crest, the SMB is anomalously low and causes arches to form in the shallow stratigraphy, observable by radar. In deeper ice, arches are consequently imprinted by both SMB and ice rheology (Raymond effect). The data show how arch amplitudes decrease as along-ridge slope increases, emphasizing that the lateral positioning of radar cross sections is important for the arch interpretation. Using the model with three rheologies (isotropic with $n=3$, 4.5 and anisotropic with $n=3$), we show that Derwael Ice Rise is close to steady state but is best explained using ice anisotropy and moderate thinning. Our preferred, albeit not unique, scenario suggests that the ice divide has existed for at least 5000 years and lowered at approximately 0.03 m a^{-1} over the last 3400 years. Independent of the specific thinning scenario, our modeling suggests that Derwael Ice Rise has exhibited a local flow regime at least since the Mid-Holocene.

1. Introduction

The knowledge of the elevation, extension, and volume history of the Antarctic Ice Sheet helps us to understand the ice sheet response to environmental forcing over millennial time scales, which contributes to better classify the changes observed in today's satellite data. For example, the gravity signal which quantifies today's mass changes must be interpreted using the glacio-isostatic adjustment, which stems from past changes in ice loading [King *et al.*, 2012]. The reconstruction of the ice sheet geometry over glacial timescales [e.g., Huybrechts, 2002; Pollard and DeConto, 2009; Whitehouse *et al.*, 2012], however, is hampered by the sparse availability of data points pertaining to the elevation history [Briggs and Tarasov, 2013]. In particular, constraints for thickness and extent of the East Antarctic Ice Sheet since the Last Glacial Maximum (LGM) are not well known, and data are mostly absent for the East Antarctic continental margin [Mackintosh *et al.*, 2014]. In our area of interest (15°E – 30°E in Dronning Maud Land), exposure dating in the Sør Rondane Mountains only provides upper boundaries of the ice sheet elevation during the LGM ($\sim 100 \text{ m}$ above present-day elevation) and the timing of the deglaciation is not known [Mackintosh *et al.*, 2014].

Outlet glaciers in Dronning Maud Land enter a comparatively small ice-shelf belt which typically extends 30–50 km from the continental shelf margin. The floating ice shelves contain a number of grounded ice rises controlling the ice flow of the tributary glaciers through buttressing. It is not known when these ice rises emerged as local flow features out of the retreating ice sheet since the LGM. We approach this question by studying the evolution of Derwael Ice Rise, an ice rise which is surrounded by Roi Baudouin Ice Shelf and which diverts the flow from Western Ragnhild Glacier, one of the biggest outlet glaciers in Dronning Maud Land [Callens *et al.*, 2014] (Figure 1). We combine geophysical data with a flow model and exploit the internal ice stratigraphy as a paleoproxy for the ice-divide residence time and for surface elevation changes. The former indicates how long the flow regime has remained local, while the latter presumably reflects changes in the ice-rise's ice-dynamic and/or atmospheric boundary conditions.

Ice on ice rises typically flows slowly from a local divide along a parabolic surface toward the margins [Martin and Sanderson, 1980]. The englacial stratigraphy records the ice-rise evolution: once a local divide is formed, deep ice beneath it deforms more stiffly under the low deviatoric stresses, and as long as the

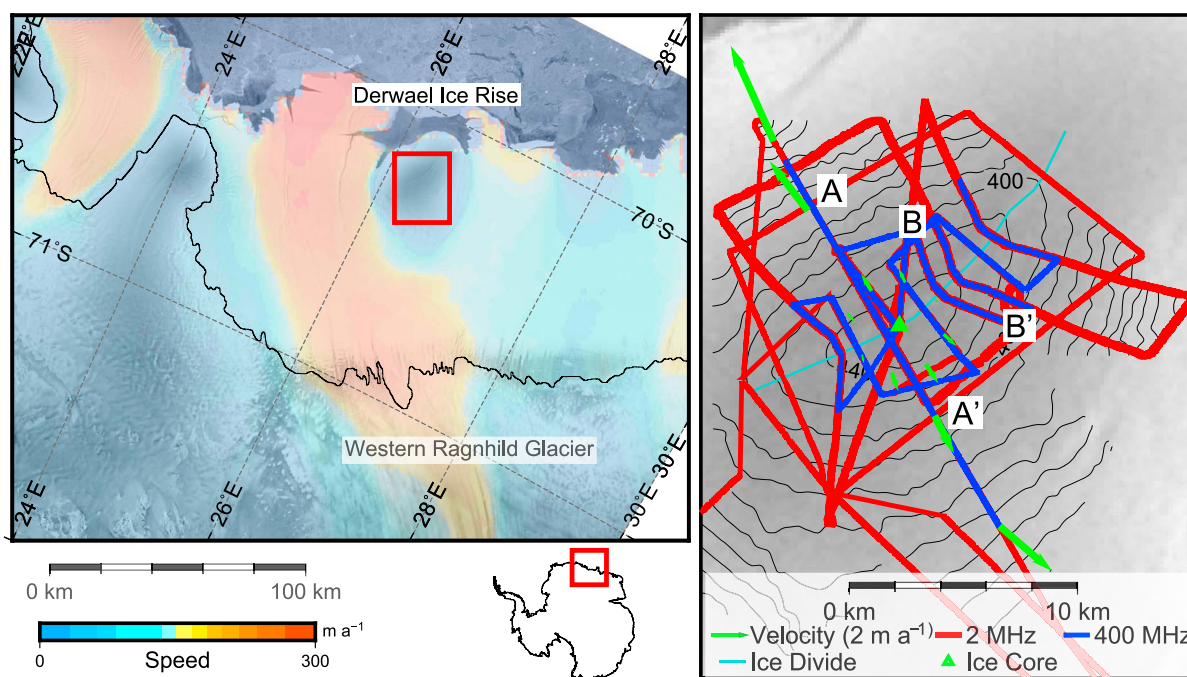


Figure 1. Derwael Ice Rise surrounded by Roi Baudouin Ice Shelf. (a) Ice-flow speed [Rignot *et al.*, 2011] illustrates that the ice rise deviates the flow from Western Ragnhild Glacier, one of the biggest outlet glaciers in Dronning Maud Land [Callens *et al.*, 2014]. Background image was taken from the Radarsat Mosaic [Jezek and RAMP-Product-Team, 2002], the grounding line in black from Bindschadler *et al.* [2011]. (b) Radar-profile locations, ice velocity, surface topography (20 m contours, meters above WGS84), and ice-core site in our study area. Data along B-B' are shown in Figure 3. Ice-flow models were applied along the flow line A-A' through the summit (Figures 9 and 11).

horizontal positioning of the divide remains stable, the stratigraphy becomes arched over time. First predicted theoretically by Raymond [1983], such arches (or Raymond Bumps) have now been visualized in the radar layering of numerous ice rises. The shape of the arches and their evolution with depth is a function of the environmental conditions that have prevailed during their formation. Important factors are the surface mass balance [Nereson and Waddington, 2002], the ice-divide residence time, and changes in surface elevation [Conway *et al.*, 1999; Martín *et al.*, 2006].

Examples for matching the radar stratigraphy of ice rises with models of varying complexity exist for Siple Dome [Nereson *et al.*, 1998, 2000; Nereson and Raymond, 2001], Roosevelt Island [Conway *et al.*, 1999; Martín *et al.*, 2006], Fletcher Promotory [Vaughan *et al.*, 1999; Gillet-Chaulet and Hindmarsh, 2011; Hindmarsh *et al.*, 2011], Halvfarryggen Ice Dome [Drews *et al.*, 2013], and Kealey Ice Rise [Martín *et al.*, 2014]. Common amongst these studies is the assumption that radar layering is isochronous, as most reflection mechanisms are linked to depositional processes at the former surface. The observed isochrones are compared with different modeling scenarios; for example, a tilt of the arch's axial plane can indicate divide migration [Hindmarsh, 1996; Nereson and Waddington, 2002; Jacobson and Waddington, 2005]. Arch amplitudes diminish with along-ridge strain rate [Martín *et al.*, 2009a] and basal sliding [Pettit *et al.*, 2003; Martín *et al.*, 2009a]. Thinning [Martín *et al.*, 2006], a higher Glen flow index [Pettit and Waddington, 2003; Martín *et al.*, 2006], and ice anisotropy [Pettit *et al.*, 2007; Martín *et al.*, 2009a] increase the arch amplitude. Repeat measurements with phase sensitive radar at Greenland Summit show that the Glen flow index n may be larger than 3 beneath divides [Gillet-Chaulet *et al.*, 2011]. Ice anisotropy on ice rises has been inferred from seismic data [Hofstede *et al.*, 2013] and sonic logging [Pettit *et al.*, 2011].

The studies mentioned above stress the sensitivity of the isochrone arch architecture to (1) the glaciological setting in which the isochrone arch is observed (e.g., surface slope, basal conditions, surface mass balance), (2) the assumed ice rheology, and (3) the history behind the isochrone arch formation. The last point contains the parameters needed to understand the ice rises's dynamic history. For a correct interpretation, however, it is imperative to also include the first two effects.

To study the evolution of Derwael Ice Rise, we represent the ice dynamics in the flow model using different rheologies and provide needed boundary conditions from the geophysical data. We use newly acquired GPS and radar data to deduce the spatial variability in surface mass balance, the bed topography, surface velocities, and the three dimensional englacial stratigraphy at all depths. After presenting the individual processing techniques and the model setup, we interpret the observational results and close by deriving the required conditions that best explain the amplitudes of the arch beneath the current divide. This sheds light on how long Derwael Ice Rise has maintained its local flow pattern, constraining the flow-history in a sector of Antarctica where little other evidence is available.

2. Regional Setting, Data, and Methods

Derwael Ice Rise faces the open ocean on the seaward side (Figure 1). It is situated in front of Western Ragnhild Glacier and causes the ice flow to bifurcate, with the majority of the ice being diverted to the west. Western Ragnhild Glacier extends hundreds of kilometers inland and progressively drains the entire catchment area [Pattyn *et al.*, 2005]. Partly due to the buttressing effect of Derwael Ice Rise, the ice stream exhibits comparatively slow surface velocities. Nevertheless, it is one of three major outlets in Dronning Maud Land, draining about 10% of the overall ice flux in the area. Near the grounding line, the glacier rests on a 65 km long, flat, and soft basin which is laterally unconstrained and well below sea level [Callens *et al.*, 2014]. This makes this particular sheet-shelf system susceptible to changes in external forcing. Variations in ice-shelf geometry and tributary flux are presumably recorded in the stratigraphy of Derwael Ice Rise.

We surveyed the ice rise in the years 2010, 2012, and 2013 with radar and GPS. During the first two campaigns, we collected kinematic GPS data to specify the surface topography. Markers were installed in 2012 and revisited in 2013 to derive ice-flow velocities (section 2.1). We acquired deep- and shallow-sounding radar profiles in 2010 and 2012; the former were used to determine bed topography and englacial structures (section 2.3) and the latter to estimate and approximate surface mass balance (section 2.3). Ice coring was undertaken in 2012. We constrain ice-flow models (section 2.4) using these field data in order to examine the evolution of the ice rise.

2.1. GPS Data for Surface Topography and Velocities

We conducted kinematic GPS surveys to determine the surface topography and positions of radar profiles, and rapid-static GPS surveys to determine ice flow. For our objectives, satellite-derived surface topography is not sufficiently accurate over many ice rises [Drews *et al.*, 2009; Wesche *et al.*, 2009], and surface velocities are too small to be detected by satellites in many cases.

In 2012 and 2013, GPS data were collected with Trimble L1/L2 receivers at 1 s intervals, simultaneously with a fixed base station at the summit. The global coordinates of the base station were fixed using static precise point positioning, the data of the remaining receivers were postprocessed differentially using the GAMIT, GLOBK/TRACK v.10.5 software package [Herring *et al.*, 2013]. In 2010, kinematic GPS data were collected at 1 s intervals using Leica L1 receivers. The data were processed using the kinematic precise point positioning from the Canadian Geodetic Survey.

Mean and standard deviation for internal cross overs from the 2010 and 2012 surveys are 0.2 ± 1.3 m and 0.0 ± 0.1 m, respectively. The lower deviations for the 2012 data reflect the more advanced processing with the dual-phase receivers. External cross-over errors for the topographic profiles in 2010 and 2012 are 0.1 ± 2.6 m. The uncertainty of ± 2.6 m is likely linked to differences in the global solutions of the precise point positioning of the different years and also at least partly reflect the interannual variability in surface elevation.

For static measurements in 2012 and 2013 (used for the surface velocities), twelve 3 m long stakes were installed in a 2 km radius around the dome and along the central radar profile (A–A', Figure 1). The GPS antennas were mounted on top of the stakes, and occupied for at least 30 min. The processing included GPS dual frequency observables, precise GPS orbits, absolute phase center corrections for the ground and satellites antennas, tropospheric refraction modeling (and estimation) and ocean loading and earth tides [e.g., Bergeot *et al.*, 2009]. The static processing was performed in two steps. First, the daily coordinates of the base station were estimated from 24 h data using the Precise Point Positioning Atomium software [Defraigne *et al.*, 2008]. The resulting position has 2 cm precision (3 sigma). Second, we estimated every baseline length in a network approach with fixed base station coordinates (the daily motion of the base station is within a

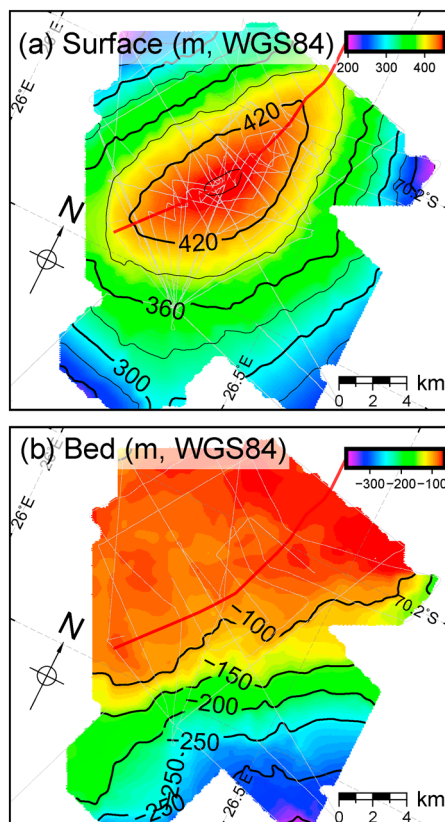


Figure 2. Interpolated maps of (a) surface elevation and (b) bed. The red curve indicates the divide position, and gray lines mark the profiles used for the interpolation.

model [Arthern *et al.*, 2010]. The model was fitted to the measurements, assuming a steady state densification and using the activation energy for grain growth E_g as a tuning parameter ($E_g = 41 \text{ kJ mol}^{-1}$, which is close to the values given in Cuffey and Paterson [2010, p. 40]). Lateral variations in density were neglected.

The englacial radar layers were dated by linking the layer depth to the ice core's tentative age–depth scale (based on $\delta^{18}\text{O}$ measurements, M. Philippe, personal communication, 2014). The ice-equivalent depth of the radar reflector divided by the layer age results in the layer-depth SMB, which is mapped spatially along the radar profiles. The internal-reflection horizon used here is dated to 21 years before 2012. More details for this approach can be found in Eisen *et al.* [2008].

We consider errors in linking the radar reflector to the tentative depth–age scale to be ± 1 year. The error in fitting the depth–density scale was calculated out of the misfit between the discrete ice-core samples and the density model (in a least square sense). Using standard error propagation, this results in a lower-bound error of $\pm 8\%$ for the SMB. In areas where the depth–density scale varies laterally, or where dynamic deformation of the radar layers is non-negligible, the derived layer-depth is erroneous. This will be discussed in section 3.2.

2.3. 2 MHz Radar Data for Bed and Deeper Layering

Ice thickness and layering of ice at depths greater than ~ 50 m were measured using a 2 MHz radar system with resistively loaded dipole antennas [e.g., Matsuoka *et al.*, 2012] and a code-based GPS receiver. The system was towed at an average speed of $8\text{--}12 \text{ km h}^{-1}$ which resulted in a mean trace spacing of ~ 20 m. The principal steps of the postprocessing included dewow filtering, bandpass filtering, and a depth-variable gain function. To account for the spatial separation of transmitter and receiver, oblique (but straight) propagation paths to the midpoint between the receiver and transmitter were assumed. Internal reflection horizons

few millimeters and therefore negligible). The resulting positions for the 12 markers were estimated with a mean precision of 0.8 and 4.3 cm for the East and North components, leading to a processing uncertainty on the velocities of 5 cm a^{-1} (3 sigma). Errors reported above are purely from the GPS analysis and do not include errors associated with tilts of the markers. Nevertheless, marker velocities along the center line (A–A' in Figure 1) range within 2 m a^{-1} and 14 m a^{-1} and the observed tilts were small; we, therefore, consider these less well-constrained uncertainties to be negligible, and we will compare the data with an ice-flow model in section 5.

2.2. 400 MHz Radar Data for Shallow Layering and Surface Mass Balance

A 400 MHz ground-penetrating radar (GSSI: SIR 3000) imaged the upper ~ 50 m of the firn column. We used the changing depth of internal radar layers as a proxy for variations in surface mass balance (SMB). We assumed that traced layers are isochronous and that the layer depth is a function only of the local SMB and not a function of ice flow (shallow layer approximation [Waddington *et al.*, 2007]). To keep this limitation in mind, we refer to the radar-derived SMB as layer-depth SMB.

In order to convert the measured two-way travel time to depth, we parameterized the wave propagation speed as a function of firn density using the mixing formula given by Looyenga [1965]. The depth–density scale is based on discrete density measurements taken on an ice core located at the center of the survey grid [Hubbard *et al.*, 2013]. To approximate the density profile between the core samples, we used a semi-empirical compaction

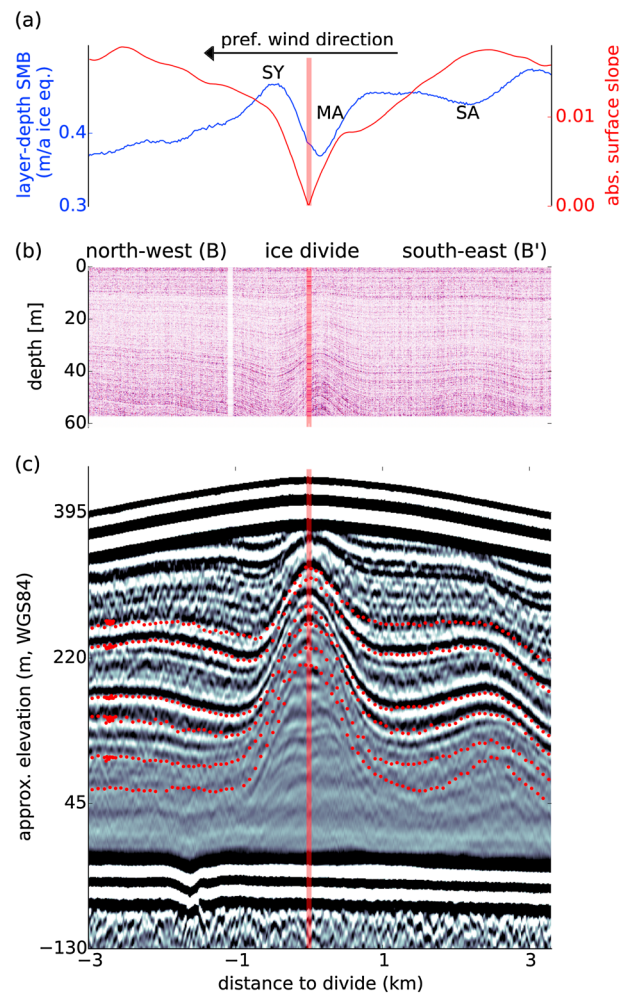


Figure 3. Radar and GPS data collected along profile B-B'. See Figure 1 for the profile location. (a) Surface slope and layer-depth SMB; interpolated map of the layer-depth SMB is shown in Figure 4. Radars that produced Figures 3b and 3c had center frequencies of 400 MHz and 2 MHz, respectively. Labels indicate the main arch (MA) with its flanking syncline (SY) and the side arch (SA) in the south-eastern flank. The red vertical bar marks the position of the topographic summit, and red dotted curves are picked radar reflectors.

were derived using line tracking of the maximum amplitude between manually picked seeds (implemented in OpendTect). We derived depths from two-way traveltimes using a uniform propagation speed ($168 \text{ m } \mu\text{s}^{-1}$). To account for the higher propagation velocity in firn, we averaged the density from the surface to the firn-ice transition (at approximately 80 m depth) and calculated the corresponding mean wave speed for firn (using the density-velocity relation from the previous section). Because all layers of the 2 MHz data are beneath the firn-ice transition, the correction for using the pure ice velocity in firn is equal for all layers and results in adding 8.8 m to the layer depths. The horizontal positioning of the code-based receiver is within a few meters which is adequate for the georeferencing of the profiles. We updated the vertical component with the differentially processed data from the L1L2 GPS (section 2.1) which was typically attached to the 400 MHz radar that occupied the same profile lines.

2.4. Model Setup

The field data are used together with a two-dimensional, full-Stokes, thermo-mechanically coupled, transient ice-flow model. The code is based on the finite element solver Elmer/Ice [Gagliardini et al., 2013] and includes implementations of isotropic and anisotropic ice rheology [Martín et al., 2006, 2009b, 2009a; Martín and Gudmundsson, 2012].

All model runs used a constant geothermal heat flux of 50 mW m^{-2} , a value which is consistent for the area of

Derwael Ice Rise in both datasets provided by Fox-Maule et al. [2005] and Purucker [2013]. We prescribed no horizontal temperature gradient at the margins, and used a constant surface temperature of -13.5°C which stems from our own measurements at 10–20 m depths. We assumed no basal sliding and the surface is allowed to evolve freely. We will consider two lateral boundary conditions: (1) a mass-conserving flux which exports the amount of ice which is equivalent to the integral over the surface mass balance from the divide to either side of the domain [Schott-Hvidberg, 1996] and (2) an elevated flux resulting from the mass conserving flux plus a thinning rate χ (in m a^{-1} ice equivalent). The latter causes the surface to lower, since the exported mass is out of balance with the spatially integrated surface mass balance.

Previous studies have shown that the arch amplitude is critically affected by the rheology used in the model [e.g., Martín et al., 2006; Pettit et al., 2007; Martín et al., 2009a]. No field data directly constrain ice rheology in this study. Therefore, we used three different rheological settings. The first two settings are isotropic cases with Glen’s flow index $n=3$ and $n=4.5$. The latter is based on measurements at Greenland Summit [Gillet-Chaulet et al., 2011]. The third setting is an anisotropic case with $n=3$ to account for a nonuniform alignment of ice-crystal axes. Ice anisotropy on ice rises has been inferred from seismic studies

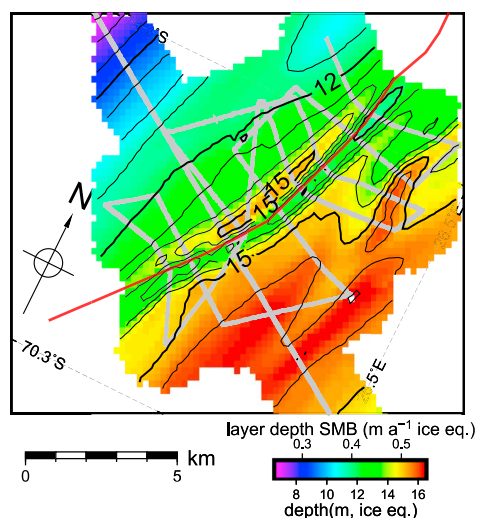


Figure 4. Interpolated depth map for a radar reflector that is dated 21 years old using the ice core collected at the summit. Corresponding SMB with shallow-layer approximation (layer-depth SMB) is shown in the color bar. Gray curves indicate radar profiles used for the interpolation. The red curve marks the divide position. This map covers a smaller area than the surface and bed maps in Figure 2.

has 400 cells in the horizontal, which corresponds to a grid spacing of 40 m. $l(n=3)$ and $l(n=4.5)$ have 40 cells in the vertical (~ 14 m at the dome). To improve computational efficiency for $A(n=3)$, we reduced the number of cells in the vertical to 30 (~ 18 m at the dome).

3. Observations

3.1. Surface and Bed Topography

Figure 2a illustrates the surface topography with a clear peak (~ 435 m above sea level) at the center. Along the divide, the surface slope is steeper toward the south-west compared to the north-east. On other ice rises, *Goodwin and Vaughan* [1995] identified double ridges which correspond to elongated depressions in the surface profile on either side of the divide. The double ridges appear in satellite imagery as dark lineations accompanying the main divide. *Martin et al.* [2009b] interpret the double ridges as a feature which evolves over time as a consequence of ice anisotropy. We find no evidence for a double ridge at Derwael Ice Rise in either the elevation model (Figure 2a) or in individual cross profiles (the slope for an exemplary cross profile is displayed in Figure 3a). The bed in Figure 2b is smooth and below sea level. It exhibits a small plateau in the vicinity of the dome and descends toward the south. The gridding for both the surface and bed is based on a nearest neighbor algorithm.

3.2. Shallow Stratigraphy

The 400 MHz radar data show continuous radar reflectors, which include four prominent features (Figure 3). First, the reflectors are generally deeper in the south-eastern flank compared to the north-western flank. Second, the reflectors arch upward at about 100–200 m offset from the topographic divide (main arch, MA, in Figure 3). This feature is visible at depths greater than 10–20 m. Third, the arch is asymmetric. There is a syncline (SY in Figure 3) in the north-east next to the main arch with no counterpart in the south-west. Fourth, there is a smaller arch 1–3 km away from the divide toward the south-east (side arch, SA, in Figure 3). The side arch has smaller amplitudes than the main arch.

A near surface layer (~ 21 years before 2012) was picked in all 400 MHz lines and gridded to produce Figure 4. For the gridding, we used ordinary kriging to better approximate the directionality of the arches. Outside of an approximately 2 km wide corridor centered at the divide, the layer depth exhibits a comparatively smooth pattern. The depths on the north-western flank are up to 50% lower compared to the south-eastern flank. The ice divide is the boundary between the two regimes. Inside the 2 km corridor, the

[*Hofstede et al.*, 2013], sonic logging [*Pettit et al.*, 2011], and also linked to the double-peaked arches at greater depths [*Martin et al.*, 2009a; *Martin and Gudmundsson*, 2012]. Hereafter, we refer to these three settings as $l(n=3)$, $l(n=4.5)$, and $A(n=3)$, respectively. For $A(n=3)$, we initialized the model with an isotropic crystal orientation fabric which evolves with ice dynamics. We used fabric-evolution parameters given by *Martin et al.* [2009a] that are compatible with laboratory measurements by *Pimienta et al.* [1987].

In preliminary runs, the steady state surface was matched to the observations by multiplying the temperature-dependent rate factor with a constant c ($c=1.0$ for $l(n=3)$, $c=8 \times 10^{-8} \text{ Pa}^{-1.5}$ for $l(n=4.5)$, and $c=0.5$ for $A(n=3)$). For $l(n=4.5)$ c changes units to account for the higher exponent in the Glen-type flow law. The scaling is equivalent to $l(n=3)$ for stresses of 0.5 bar. The constants were then set and did not evolve through the computations.

The model domain is centered at the divide and extends 8 km (about 15 ice thicknesses) in both directions. The initial geometry is based on the bed and surface elevation from our own data. The mesh

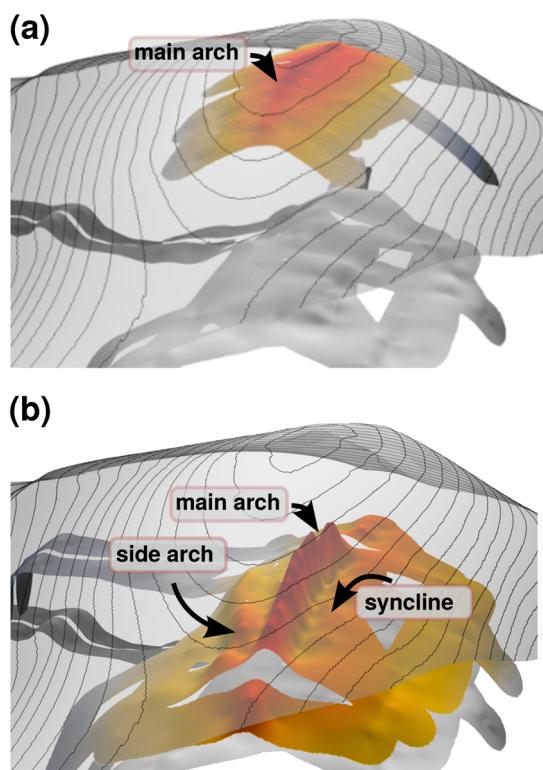


Figure 5. Spatial interpolation of the englacial stratigraphy at average depths of (a) 30 m and (b) 300 m. The surface and bed topography are shown in gray. Viewing angle is from the north-east along the divide.

arches near the divide and the synclines in the north-east constitute an elongated wave-like pattern extending near-parallel to the crest. The amplitude of this oscillation decreases with increasing distance from the surface peak (Figure 5a).

The side arch in the shallow layering is at kilometer 2 in Figures 3a and 3b and emerges as an elongated minimum in the south-eastern flank of the interpolated layer-depth (Figure 4). It is oriented in the north-south direction. The distance of the arch maxima observed at the different cross sections is greater on profiles closer to the main flowline through the summit. The side arches continue at intermediate depths in the 2 MHz data and increase in amplitude.

3.3. Deep Stratigraphy

Figure 3c is an example for the 2 MHz radarograms (along B-B; Figure 1). Similar to what is observed in the shallow layering, the central arch is accompanied by a flanking syncline in the north-western flank. On the other side, the side arch gets more evident with increasing depth. It is smaller in amplitude than the main arch, and its axial plane is tilted toward the divide.

We traced six englacial reflectors that connect all 2 MHz radar data. Figure 5b visualizes an interpolated radar reflector. Along all divide-across profiles, the main arch was observed within 200 m of the topographic divide position. The syncline feature is prominent in the north-western side of the divide and decays together with the main arch with increasing distance from the summit. The side arch appears in multiple cross profiles, and (similar to what was observed for the shallow layers) the distance between the main and side arches is greater on profiles closer to the main flowline through the summit.

Figure 6 illustrates the main arch’s amplitude versus relative depth distribution for all cross sections. The amplitude is defined as the vertical distance between the arch maximum and a point in the flank (chosen

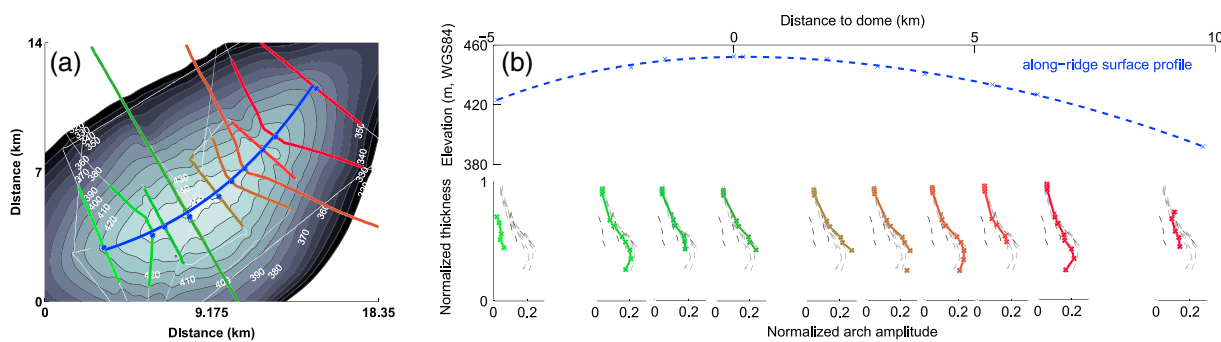


Figure 6. Along-ridge variations of the main-arch amplitudes. Illustrated are (a) the radar profiles on the map with colors corresponding to (b) the depth profiles of the normalized arch amplitudes (depth and amplitude are relative to the local ice thickness). The gray curves are the amplitude–depth curves collected on all 10 cross profiles. These are plotted as a reference for the individual cross profiles.

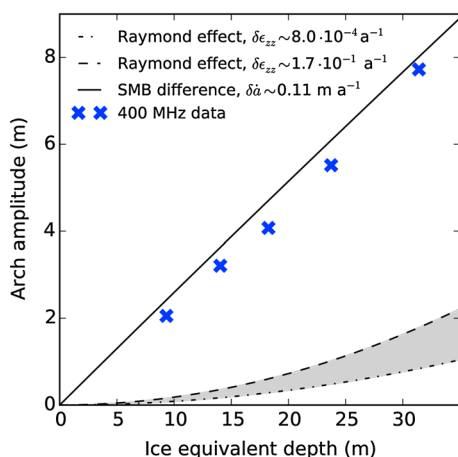


Figure 7. Arch amplitude variations along depth obtained from measurements (cross markers), and theoretical predictions for SMB-caused arches (solid line) and arches caused by the Raymond effect (dashed curves) after Vaughan et al. [1999].

if they originate from differences in SMB ($\delta\hat{a}$, equation (4) in Vaughan et al. [1999]) and quadratically with depth, if they originate from ice rheology (i.e., spatial variations in vertical strain rates $\delta\dot{\epsilon}$; equation (5) in Vaughan et al. [1999]).

Figure 7 shows that the observed shallow arches grow linearly with depth. The trend is similar to an SMB driven scenario, for which we assumed $\delta\hat{a} \sim 0.11 \text{ m a}^{-1}$ based on the layer-depth SMB from section 2.2. The rheology-case underestimates the arch amplitudes. Here we considered $\delta\dot{\epsilon} = 8 \times 10^{-4} \text{ a}^{-1}$ (for Derwael Ice Rise being in steady state) and $\delta\dot{\epsilon} = 1.7 \times 10^{-3} \text{ a}^{-1}$ (for the case where the ice rise is thinning). Those values are based on the computations in the following section 5. We conclude that the layer-depth SMB is the primary cause for the shallow arches near the divide, reflecting a SMB minimum near the divide on the upwind side which is accompanied by a SMB maximum at the downwind side. The observed arch amplitudes are slightly larger than the SMB-based prediction and other mechanisms (e.g., the Raymond effect or temporal SMB variations) may play a subordinate role in the arch formation.

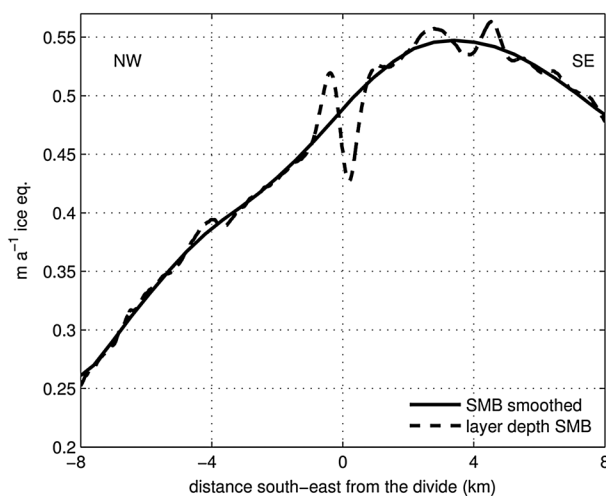


Figure 8. SMB patterns inferred from profile line A-A' used for the modeling. The smoothing artificially excludes the SMB oscillation near the divide.

2 km away from the divide on the north-western flank). All values are normalized to the local ice thickness. The largest amplitudes, 25% of the ice thickness, are encountered near the dome. In cross sections farther away from the dome, the amplitudes are increasingly damped.

4. Present-Day Surface Mass Balance

We estimated the recent SMB averaged over the past 21 years using a radar reflector dated with the ice core (Figure 4). This analysis presupposes that the depth of shallow radar reflector depends on the SMB only. However, deeper reflector are also affected by ice deformation (e.g., the Raymond effect) [Waddington et al., 2007], which may erroneously propagate into the layer-depth SMB causing the elongated oscillation near the divide. To evaluate these two contributions for the formation of shallow arches at the divide, we applied a test presented by Vaughan et al. [1999].

They show that arches grow linearly with depth,

5. Numerical Modeling of the Main Arch Amplitudes

From this point on, we will focus on the main arch beneath the dome. The goal is to derive a set of conditions (required time scales, rheological properties, thinning/thickening rates) using an ice-flow model. This will help to better understand the characteristics of the other observed features in the ice stratigraphy (i.e., flanking syncline, double-peaked arches, and the side arch).

5.1. Modelled Arch Amplitudes for Steady State Conditions

In order to minimize the effects of along-ridge strain-rates, we apply the two-dimensional model along a flowline across the dome (A-A', Figure 1). We first examine the arch amplitudes for steady

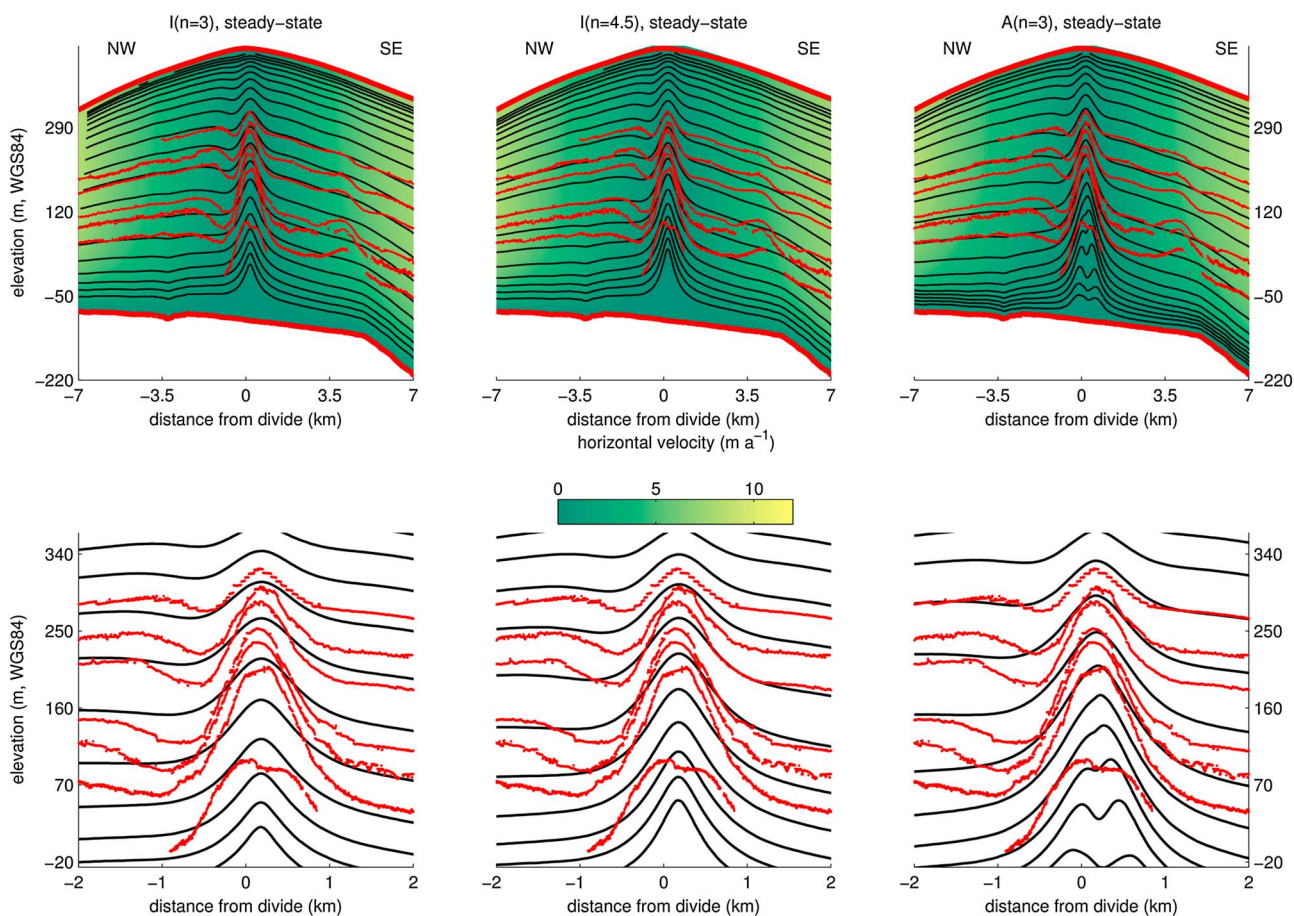


Figure 9. Comparison of data and steady state model outputs along the A-A' profile (Figure 1): The three panels on the top show the results for different rheologies and no thinning. The horizontal velocities are color coded and modeled isochrones in black. The red curves correspond to the 2 MHz radar reflectors. The lower panels enlarge areas closer to the divide.

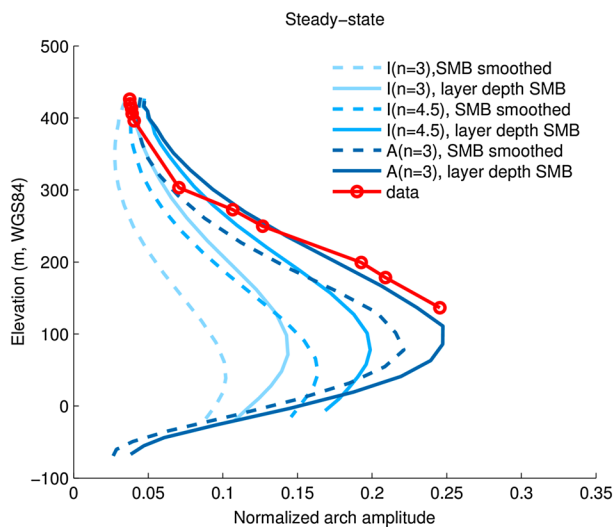


Figure 10. Modeled, steady state arch amplitudes for both SMB patterns shown in Figure 8. Dashed curves show the results for the smoothed SMB, and solid curves for the layer-depth SMB.

state conditions by applying the mass-conserving boundary conditions at the downstream model boundaries. We consider the three rheologies $l(n=3)$, $l(n=4.5)$, and $A(n=3)$. The model is run to $10t_d = 10,000$ a after which the arches reach steady state (i.e., individual layers get older, but the age-depth pattern remains unchanged).

We use the spatial SMB pattern derived in section 4. Because the ice core shows that the 114 year averaged SMB is only 70% of the 21 year averaged SMB [Hubbard et al., 2013; M. Philippe personal communication, 2014], the SMB is scaled with a constant (0.7) to match the long-term average at the site. To examine the effects of neglecting the small-scale SMB anomaly near the summit, we also consider a smoothed version of the (scaled) SMB (Figure 8).

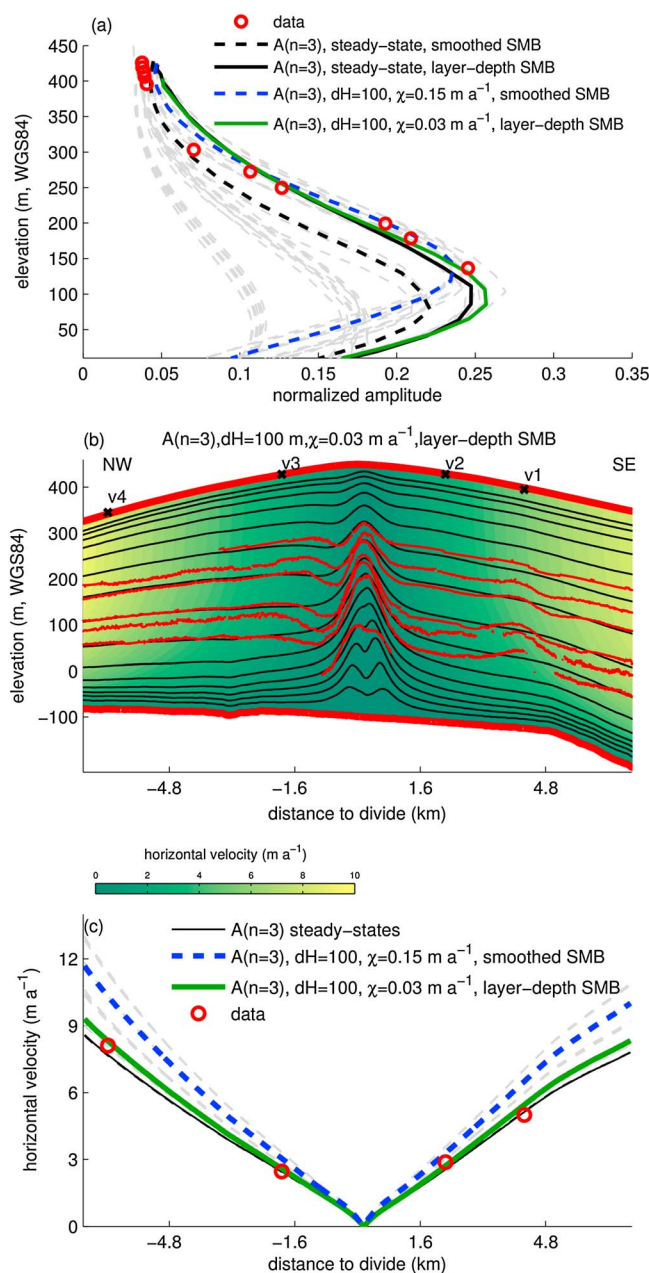


Figure 11. Transient model results. (a) Depth profiles of the main arch amplitudes for all transient model cases and for observations (red). Thinning is sustained for approximately $\frac{dH}{\chi}$ years. (b) Modeled isochrones and flow speed (background color) for the preferred scenario using the layer-depth SMB with $A(n=3)$, $dH = 100$ m and $\chi = 0.03$ m a⁻¹ together with observed radar reflectors (red). (c) Modeled horizontal flow speeds for the best matching steady state (black), and transient scenarios using the layer-depth SMB (green) and the smoothed SMB (blue) compared to the GPS measurements.

fully evolved but still smaller than the ones observed in deeper ice (Figure 10). We, therefore, consider the possibility that Derwael Ice Rise was thicker in the past (with correspondingly larger arch amplitudes) and has thinned since to its current geometry. Such a scenario can improve the match between the simulated and the observed arch amplitudes.

Figure 9 displays the steady state results for the layer-depth SMB. We compare the radar reflectors with the isochrones of the modeled age field. All three cases match the internal radar layering in the flanks reasonably well, albeit the three deeper radar reflectors in the south-eastern high-SMB regime appear systematically lower than the modeled isochrones. The flanking synclines (around kilometer -1) in the model are too small and the remnants of the side arch (around kilometer 4) have no counterpart in the modeled age fields. The arch amplitudes increase with increasing n , but the isotropic models result in arch amplitudes that are too small at all depths. The best fit is obtained with $A(n=3)$.

In a second steady state experiment, we use the smoothed SMB. In results not shown here, we find that in that case the flanking synclines in the north-west are absent in the age fields. Because arches are solely induced by ice rheology (and not SMB), the arch amplitudes are significantly smaller and largely deviate from the observations (Figure 10, dashed curves).

The arch amplitudes are best approximated for steady state conditions using $A(n=3)$ in combination with the layer-depth SMB. This setup produces larger double-peaked isochrone arches than the ones foreshadowed by the lowest radar reflector and also develops a double ridge at the dome (after approximately 3000–4000 years) which is not observed in the present-day surface topography (section 3.1). This suggests that Derwael Ice Rise is not yet in steady state, meaning that the internal ice stratigraphy and the surface have not yet completely adjusted to the current geometry. The modeled amplitudes, on the other hand, are

5.2. Modeled Arch Amplitudes for Transient Conditions

We use both SMB patterns displayed in Figure 8 and initialize as described above with the exception that prior to the evolution, a constant ice thickness dH is added. This simulates a thicker ice rise with the same surface and bed geometry as Derwael Ice Rise. We evolve this ice rise to steady state ($10t_d$) using the mass-conserving boundary condition. The absolute arch amplitudes are now larger because the ice rise is thicker. In the following step, the SMB is kept constant, but the thinning rate χ is added to the SMB within the integral that defines the flux boundary condition at the sides. This causes an imbalance of the incoming and outgoing mass fluxes, and lowering of the surface. We refer to these runs as transient. Since the internal stratigraphy does not adjust immediately to the new geometry, thinning results in larger isochrone arches than those in the corresponding steady state scenario with a constant ice thickness.

For the smoothed SMB scenario, we consider values for dH of 200, 280, and 360 m and thinning rates χ of 0.03, 0.09, 0.15, and 0.21 m a^{-1} . Because arch amplitudes are larger when using the layer-depth SMB, we investigate smaller values for dH (50 and 100 m) and χ (0.015, 0.03, and 0.09 m a^{-1}) for this case. The transient simulations are computed for the three rheologies mentioned above and stopped when the modeled surface matches the presently observed surface in a least-squares sense (approximately after dH/χ years).

Figure 11a displays the modeled arch amplitudes on profile A-A' for all cases. There are three expected characteristics which are largely independent of rheology and SMB:

1. Increasing values of dH (and χ to a lesser extent for the ranges considered here) increase the final arch amplitudes. This is inherent to the model setup as a larger dH produces large amplitudes to start with. The considered thinning rates are too fast for the internal stratigraphy to adapt to the new geometry; hence, the arches are oversized.
2. As χ increases, the maximum arch amplitudes appear at shallower depths.
3. The surface velocities increase with χ and are virtually independent of dH , which is a direct consequence of mass conservation.

The $l(n=3)$, $l(n=4.5)$ cases result in amplitudes that are too small regardless of the applied SMB pattern. For the smoothed SMB and $A(n=3)$, the amplitudes are slightly underestimated for $(dH, \chi)=(280 \text{ m}, 0.15 \text{ m a}^{-1})$ and slightly overestimated for $(dH, \chi)=(360 \text{ m}, 0.15 \text{ m a}^{-1})$. In this scenario, the surface velocities are too fast compared to the observations. When using the layer-depth SMB and $A(n=3)$, we find the best match for $(dH, \chi)=(100 \text{ m}, 0.03 \text{ m a}^{-1})$ (Figure 11b). This case approximates the measured surface velocities best (Figure 11c).

6. Discussion

6.1. Spatial Variations of SMB

The spatial gradient of the SMB is well constrained by our radar data on the ice-rise flanks. Similar SMB patterns have been observed on other ice rises [Nereson *et al.*, 2000; King *et al.*, 2004; Drews *et al.*, 2013]. In all cases, higher SMB values were found on the upwind side. Atmospheric modeling suggests that this pattern is caused by orographic uplift from moist air on the upwind slopes and a precipitation shadow on the downwind slopes [Lenaerts *et al.*, 2014]. This is consistent with the signal in the layer-depth SMB derived here (Figure 4). Given the evidence from both atmospheric modeling and multiple on-site observations, it appears that this type of SMB pattern is a generic feature of ice rises which are subject to preferred wind directions.

In a small zone near the divide, we find shallow synclines and anticlines in the radar layers which imprint the layer-depth SMB (Figure 8). The analysis of section 4 indicates that this pattern indeed reflects a SMB minimum near the divide and a SMB maximum at the down-wind side. The arch minima are offset to the divide by a few hundred meters to the up-wind side, though Raymond Arches develop exactly at the crest position in a steady state. A similar offset between arch peak and divide position has been observed in the shallow radar layers of nearby Halvfarryggen Ice Dome (Figure 5 in Drews *et al.* [2013]). The spatial resolution of atmospheric models (e.g., 5 km in Lenaerts *et al.* [2014]) is too coarse to resolve this effect, but conceivable mechanisms are wind erosion near the crest and subsequent redeposition at the divide's down-wind side. This result is contrary to what is reported by Vaughan *et al.* [1999] for Fletcher Promontory and Conway *et al.* [1999] for Roosevelt Island, both stating that there is no evidence for wind erosion at the crest for those ice rises. It is yet unclear why some ice rises show this SMB anomaly and others do not. Nevertheless, the local

anomalies of SMB near the crest affect the simulated arch amplitudes from the surface down to 70% depth (Figure 10). The magnitude of the SMB anomaly should be well-known for studies using the arch amplitudes to study the ice-rise evolution.

6.2. Interpretation of the Main Arch Metrics

Figure 6 is observational evidence for the sensitivity of the arch amplitudes to along-ridge slope as previously discussed in a modeling study [Martín *et al.*, 2009a] (assuming that along-ridge strain rate increases with increasing along-ridge slope): At kilometer +5 away from the summit (along-ridge slope ~ 0.0058), the upward arching is still pronounced, whereas at kilometer -5 , it is basically absent (along-ridge slope ~ 0.012). This illustrates the importance of taking the lateral positioning of the cross sections into account when interpreting the arch amplitudes (particularly in studies where only few cross profiles are available). The dependency on the along-ridge slope also hampers a detailed comparison with other ice rises where the surface topography is often less well known. A gross comparison shows that the normalized amplitudes (both depth and amplitude normalized to the local ice thickness) observed here are larger than at Roosevelt Island [Martín *et al.*, 2006], Siple Dome [Nereson and Raymond, 2001], Halvfarryggen Ice Dome [Drews *et al.*, 2013], and Kealey Ice Rise [Martín *et al.*, 2014]), and comparable to Fletcher Promotory [Hindmarsh *et al.*, 2011], and Fuchs Piedmont [Martín *et al.*, 2006].

Our two-dimensional model assumes neither off-profile flow nor basal sliding. The former is justified because the modeling domain crosses the summit and is aligned perpendicular to the surface contours. The topography is well constrained by the GPS data, and we expect little ice-flow across the modeling domain near the dome. The second assumption strongly depends on the magnitude of the geothermal flux. However, the values we chose are consistent in different data sets [Fox-Maule *et al.*, 2005; Purucker, 2013], and the simulated basal temperatures (approximately -5°C) are well below the pressure melting point. We are therefore confident that these model simplifications do not seriously affect our interpretations of the arch amplitudes.

All isotropic, steady state simulations underestimate the main arch amplitudes, regardless of the applied SMB (Figure 11a). We get a best fit for $A(n = 3)$ in combination with the layer-depth SMB which produces slightly smaller amplitudes at larger depths than the observed ones. The analysis in section 5.1 suggests that Derwael Ice Rise may not yet fully be in steady state because (1) modeled double-peaked arches are larger than the observed one, (2) the modeled double ridge at the surface is absent in the data, and (3) because the modeled arch amplitudes are smaller than the observed ones in deeper ice. According to our model, the double-peaked arches first appear 1500 years after the onset of divide-flow, and the double ridge is visible after 3000–4000 years. At those time intervals, the amplitudes at intermediate depths are smaller than the steady state ones and hence deviate more from our observations.

The transient simulations cover a time period for thinning over 600–12000 years. We find the best match using the layer-depth SMB and $A(n=3)$, with a thinning rate of 0.03 m a^{-1} over 3400 years ($dH = 100 \text{ m}$). Using the (less plausible) smoothed SMB, we find good matches for $A(n=3)$ with thinning rates of 0.15 m a^{-1} over 1900–2500 years ($dH = 280\text{--}360 \text{ m}$). Compared to the steady state computations, the transient results improve the match to the observed arch amplitudes (Figure 11a).

It is less evident to constrain the exact value of the thinning as well as its time period based on the isochrone arches only. The deduction is not unique in terms of temporal SMB changes, ice-rheology, and various combinations of dH and χ . In the transient runs, the artificially elevated ice rise was fully evolved before the thinning started. This resembles an ice rise that always exhibited a local flow regime. Similarly, we could start from a flat surface and thin simultaneously with the onset of the divide formation, a type of scenario that would be expected from an ice rise emerging out of a retreating ice sheet [c.f., Conway *et al.*, 1999]. In that case, the arch amplitudes would evolve simultaneously with the onset of thinning and larger values of dH would be needed compared to the case above (in which the amplitudes are fully evolved prior to the commencement of thinning). Larger values of dH are also needed when using isotropic rheologies, which principally result in smaller amplitudes.

The thinning scenario with $\chi = 0.03 \text{ m a}^{-1}$ best matches the measured surface velocities (Figure 11c), but differences compared to the steady state results are not significant, particularly regarding the uncertainties in the long-term average of the SMB (which critically impacts the modeled velocities via the lateral boundary conditions). The effect of using the smoothed SMB becomes evident here, because it requires

higher thinning rates to match the arch amplitudes which results in too large surface velocities compared to the observations.

The observed radar stratigraphy and surface velocities are best approximated with $A(n=3)$ and an ice rise that has thinned by 0.03 m a^{-1} over the past 3400 years. Steady state experiments with $A(n=3)$ also replicate most of observed features. External evidence for the thinning hypothesis comes from repeat-pass observations of the Envisat radar altimeter which detects an averaged thinning rate of 0.08 m a^{-1} in a 10 km radius around the dome of Derwael Ice Rise for the time period of 2002–2012 [Flament and Rémy, 2012]. Even though the time interval of the satellite observations is small compared to the characteristic time of Derwael Ice Rise, we conclude that scenarios with small thinning rates for Derwael Ice Rise best explain the observations.

In order to explain the observed arch amplitudes, both steady state and transient scenarios require a local divide which remained horizontally stable for multiple millennia. Our preferred scenario (layer-depth SMB, $A(n=3)$, $dH = 100 \text{ m}$, $\chi = 0.03 \text{ m a}^{-1}$) needs a horizontally stable divide for at least 5000 years (3400 years of thinning, and prior to that, at least 1600 years for the initial development of the arches). Steady state simulations have a comparable lower boundary for the ice-divide stability. We hence conclude that Derwael Ice Rise has remained as a local flow feature during that time period, and was not at all, or at least not entirely overrun by the continental Antarctic Ice Sheet. Yamane *et al.* [2011] infer from exposure dating in the Lützow-Holm Bay region (approximately 500 km eastward of Derwael Ice Rise) that the East Antarctic Ice Sheet retreated between 10 ka to 6 ka ago, with a change of ice thickness of at least 350 m. A glacial ice sheet which was a few hundred meters thicker than today and which retreated and thinned in the Early to Middle Holocene can also explain our observations here. However, in our model the thinning is prescribed and does not appear as a consequence of changing boundary conditions in the surrounding ice shelf. The interaction with the surrounding is therefore not well captured and requires more investigation.

6.3. Proposed Cause for the Side Arch

There are no features in the 3-D bed topography which relate to the side arch (Figure 2b). The layer-depth SMB does show an anomaly in this area (Figure 8 at kilometer 4), but there is no corresponding structures of isochrones at greater depths (Figures 9 and 10b). A possible hypothesis is that the side arch is an expression of a past divide migration. If a former divide was stable enough for an isochrone arch stack to evolve, a migration of the divide to its current position would result in remnant arches in the flank which are advected and decay over time [Waddington *et al.*, 2001; Nereson and Waddington, 2002; Jacobson and Waddington, 2005]. The advection velocities are primarily a function of surface slope, which explains the remnant side arch occurring at a variable distance from today's divide. The observed tilt of the side arch's axial plane toward today's divide suggests that the migration cannot be abrupt because the remnant stack would then tilt away from the divide (due to the faster advection near the surface compared to near the bottom). Assuming that the main arch requires a stable divide for at least 5000 years, however, it is difficult to link both arches quantitatively using simple migration scenarios. For example, assuming a mean horizontal advection of 2 m a^{-1} (as a lower boundary) over 5000 years results in a lateral displacement of approximately 10 km, but the largest distance to today's divide is only about 4 km. Due to the absence of other mechanisms, we still interpret the side arch as a remnant arch from a former divide migration, albeit the specific scenario may contain parameters which have not been considered so far (e.g., a secondary divide, different thinning scenarios with migration and/or spatial and temporal changes in SMB).

7. Summary and Conclusions

We present geophysical data imaging the surface, bed, englacial stratigraphy, and flow velocities of Derwael Ice Rise. We combine the data with an ice-flow model to study the ice-rise evolution. Arches in the radar stratigraphy are consistently found in all profiles across the divide. Arches develop at approximately 20 m depth, and in some profiles they show double-peaks in deep ice. Our data show the decrease of arch amplitudes with increasing along-ridge slope, illustrating that multiple cross sections are needed to find the largest arch amplitudes, particularly on ice rises where the topography is not well known and/or where the summit position has migrated.

We deduce a topography-driven surface mass balance gradient, which originates from orographic uplift of moist air on the south-eastern flank and a corresponding precipitation shadow in the north-western flank. The SMB exhibits a local minimum a few hundred meters offset to the up-wind side of the topographic

divide, and a local SMB maximum 1 km farther away on the down-wind side. This suggests SMB effects (e.g., wind-scouring and subsequent redeposition) on scales which are currently undersampled in atmospheric models. The impact of a local SMB minimum on the arch formation has been considered previously in theoretical studies [Nereson and Waddington, 2002], but so far no observational data has been included in a study regarding ice-rise evolution. On the contrary, Vaughan *et al.* [1999] and Conway *et al.* [1999] found no evidence for an SMB minimum near the divide and further investigation is warranted. Regardless of the specific mechanism, the observed SMB anomaly in our study crucially imprints the modeled arch amplitudes from the surface down to 70% depth. The effect has a similar magnitude as the three different rheologies applied here.

We use the three ice rheologies, the SMB anomaly near the divide, and various thinning rates to model the arch amplitudes beneath the dome. Within this set of simulations, the arch amplitudes are adequately matched in a steady state scenario with anisotropic rheology but best explained using transient simulations with moderate thinning. Our preferred scenario contains an anisotropic rheology and a fully evolved ice rise which was 100 m thicker than today, and which lowered at 0.03 ma^{-1} over the last 3400 years. This scenario is nonunique, and other combinations of thinning rates and thinning time intervals also approximate the observations. Although the time intervals are different and therefore may encompass different mechanisms, the thinning in general accords with observations from satellite altimetry averaged over ten years [Flament and Rémy, 2012].

Independent of thinning, all scenarios investigated here require that the horizontal position of the ice divide has remained stable for multiple millennia (likely more than 5000 years). This suggests that Derwael Ice Rise has maintained its local flow field and was not overrun by the continental Antarctic Ice Sheet during that period.

Acknowledgments

Financial support to R. D. is given by the FNRS-FRFC (Fonds de la Recherche Scientifique) IDyRA project and for D. C. by a FNRS-FRIA fellowship. Field work in 2010 was part of the BELISSIMA project funded through the Belgian Science Policy Office (BELSPO). Field work in 2012 and 2013 was funded by the InBev-Baillet Antarctica Fellowship and the BELSPO project ICECON. The logistics were organized by the International Polar Foundation. Radar work was supported by the Center for Ice, Climate, and Ecosystems of the Norwegian Polar Institute. A research visit for R. Drews at the British Antarctic Survey, Cambridge, was financed by FNRS (Crédit Bref Séjour à l'étranger). GPS Processing was done using GAMIT/GLOBK developed by the Massachusetts Institute of Technology, Scripps Institution of Oceanography, and the Harvard University. The finite element modeling is based on the open-source code Elmer mainly developed by the CSC-IT Center for Science Ltd in Finland. Data from the ice core were provided by M. Philippe and J. L. Tison from the Laboratoire de Glaciologie at ULB. Joel Brown gave valuable insights for the GPS and Radar processing. Pascale Defraigne provided the GPS coordinates for the base station using the PPP Atomium software. We acknowledge constructive input from Erin Pettit, Ed Waddington, Neil Ross, and Robert Bingham on an earlier version of this paper. Data collected in this study are available on PANGAEA.

References

- Athern, R. J., D. G. Vaughan, A. M. Rankin, R. Mulvaney, and E. R. Thomas (2010), In situ measurements of Antarctic snow compaction compared with predictions of models, *J. Geophys. Res.*, *115*, F03011, doi:10.1029/2009JF001306.
- Bergeot, N., M. N. Bouin, B. Diament, M. Pelletier, M. Régner, S. Calmant, and V. Ballu (2009), Horizontal and vertical interseismic velocity fields in the Vanuatu subduction zone from GPS measurements: Evidence for a central Vanuatu locked zone, *J. Geophys. Res.*, *114*, B06405, doi:10.1029/2007JB005249.
- Bindschadler, R., *et al.* (2011), Getting around Antarctica: New high-resolution mappings of the grounded and freely-floating boundaries of the Antarctic ice sheet created for the International Polar Year, *Cryosphere*, *5*(3), 569–588, doi:10.5194/tc-5-569-2011.
- Briggs, R. D., and L. Tarasov (2013), How to evaluate model-derived deglaciation chronologies: A case study using Antarctica, *Quat. Sci. Rev.*, *63*, 109–127, doi:10.1016/j.quascirev.2012.11.021.
- Callens, D., K. Matsuoka, D. Steinhage, B. Smith, and F. Pattyn (2014), Transition of flow regime along a marine-terminating outlet glacier in East Antarctica, *Cryosphere*, *8*, 867–875, doi:10.5194/tc-8-867-2014.
- Conway, H., B. L. Hall, G. H. Denton, A. M. Gades, and E. D. Waddington (1999), Past and future grounding-line retreat of the West Antarctic ice sheet, *Science*, *286*(5438), 280–283, doi:10.1126/science.286.5438.280.
- Cuffey, K., and W. Paterson (2010), *The Physics of Glaciers*, 4th ed., Academic Press, Burlington, Mass.
- Defraigne, P., N. Guyennon, and C. Bruyinx (2008), GPS time and frequency transfer: PPP and phase-only analysis, *Int. J. Navig. Obs.*, *2008*, 7, doi:10.1155/2008/175468.
- Drews, R., W. Rack, C. Wesche, and V. Helm (2009), A spatially adjusted elevation model in Dronning Maud Land, Antarctica, based on differential SAR interferometry, *IEEE Trans. Geosci. Remote Sens.*, *47*(8), 2501–2509, doi:10.1109/TGRS.2009.2016081.
- Drews, R., C. Martin, D. Steinhage, and O. Eisen (2013), Characterizing the glaciological conditions at Halvfarryggen ice dome, Dronning Maud Land, Antarctica, *J. Glaciol.*, *59*(213), 9–20, doi:10.3189/2013JoG12J134.
- Eisen, O., *et al.* (2008), Ground-based measurements of spatial and temporal variability of snow accumulation in East Antarctica, *Rev. Geophys.*, *46*, RG2001, doi:10.1029/2006RG000218.
- Flament, T., and F. Rémy (2012), Dynamic thinning of Antarctic glaciers from long-track repeat radar altimetry, *J. Glaciol.*, *58*(211), 830–840, doi:10.3189/2012JoG11J118.
- Fox-Maule, C., M. E. Purucker, N. Olsen, and K. Mosegaard (2005), Heat flux anomalies in Antarctica revealed by satellite magnetic data, *Science*, *309*(5733), 464–467, doi:10.1126/science.1106888.
- Gagliardini, O., *et al.* (2013), Capabilities and performance of Elmer/Ice, a new generation ice-sheet model, *Geosci. Model Dev. Discuss.*, *6*(1), 1689–1741, doi:10.5194/gmdd-6-1689-2013.
- Gillet-Chaulet, F., and R. C. A. Hindmarsh (2011), Flow at ice-divide triple junctions: 1. Three-dimensional full-Stokes modelling, *J. Geophys. Res.*, *116*, F02023, doi:10.1029/2009JF001611.
- Gillet-Chaulet, F., R. C. A. Hindmarsh, H. F. J. Corr, E. C. King, and A. Jenkins (2011), In-situ quantification of ice rheology and direct measurement of the Raymond Effect at Summit, Greenland using a phase-sensitive radar, *Geophys. Res. Lett.*, *38*, L24503, doi:10.1029/2011GL049843.
- Goodwin, A. H., and D. G. Vaughan (1995), A topographic origin for double-ridge features in visible imagery of ice divides in Antarctica, *J. Glaciol.*, *41*(139), 483–489.
- Herring, T. A., R. W. King, and S. C. McCluskey (2013), *Introduction to GAMIT/GLOBK, Release 10.5*, vol. 48, Massachusetts Institute of Technology, Cambridge.

- Hindmarsh, R. C. A. (1996), Stochastic perturbation of divide position, *Ann. Glaciol.*, *23*, 105–115.
- Hindmarsh, R. C. A., E. C. King, R. Mulvaney, H. F. J. Corr, G. Hiess, and F. Gillet-Chaulet (2011), Flow at ice-divide triple junctions: 2. Three-dimensional views of isochrone architecture from ice-penetrating radar surveys, *J. Geophys. Res.*, *161*, F02024, doi:10.1029/2009JF001622.
- Hofstede, C., O. Eisen, A. Diez, D. Jansen, Y. Kristoffersen, A. Lambrecht, and C. Mayer (2013), Investigating englacial reflections with vibro- and explosive-seismic surveys at Halvfarryggen ice dome, Antarctica, *Ann. Glaciol.*, *54*(64), 189–200, doi:10.3189/2013AoG64A064.
- Hubbard, B., J.-L. Tison, M. Philippe, B. Heene, F. Pattyn, T. Malone, and J. Freitag (2013), Ice shelf density reconstructed from optical televiewer borehole logging, *Geophys. Res. Lett.*, *40*, 5882–5887, doi:10.1002/2013GL058023.
- Huybrechts, P. (2002), Sea-level changes at the LGM from ice-dynamic reconstructions of the Greenland and Antarctic ice sheets during the glacial cycles, *Quat. Sci. Rev.*, *21*(1), 203–231.
- Jacobson, H. P., and E. D. Waddington (2005), Recumbent folding of divide arches in response to unsteady ice-divide migration, *J. Glaciol.*, *51*(173), 201–209.
- Jezek, V., and RAMP-Product-Team (2002), *RAMP AMM-1 SAR Image Mosaic of Antarctica*, Alaska Satellite Facility, in association with the National Snow and Ice Data Center, Boulder, CO. Digital media, Fairbanks, Alaska.
- King, J. C., P. S. Anderson, D. G. Vaughan, G. W. Mann, S. D. Mobbs, and S. B. Vosper (2004), Wind-borne redistribution of snow across an Antarctic ice rise, *J. Geophys. Res.*, *109*, D11104, doi:10.1029/2003JD004361.
- King, M. A., R. J. Bingham, P. Moore, P. L. Whitehouse, M. J. Bentley, and G. A. Milne (2012), Lower satellite-gravimetry estimates of Antarctic sea-level contribution, *Nature*, *7425*, 586–589, doi:10.1038/nature11621.
- Lenaerts, J. T. M., et al. (2014), High variability of climate and surface mass balance induced by Antarctic ice rises, *J. Glaciol.*, *60*(224), 1101–1110, doi:10.3189/2014JoG14J040.
- Looyenga, H. (1965), Dielectric constants of heterogeneous mixtures, *Physica*, *31*, 401–406.
- Mackintosh, A. N., et al. (2014), Retreat history of the East Antarctic Ice Sheet since the Last Glacial Maximum, *Quat. Sci. Rev.*, *100*, 10–30, doi:10.1016/j.quascirev.2013.07.024.
- Martin, C., and G. H. Gudmundsson (2012), Effects of nonlinear rheology, temperature and anisotropy on the relationship between age and depth at ice divides, *Cryosphere*, *6*, 1221–1229, doi:10.5194/tc-6-1221-2012.
- Martin, C., R. C. A. Hindmarsh, and F. J. Navarro (2006), Dating ice flow change near the flow divide at Roosevelt Island, Antarctica, by using a thermomechanical model to predict radar stratigraphy, *J. Geophys. Res.*, *111*, F01011, doi:10.1029/2005JF000326.
- Martin, C., R. C. A. Hindmarsh, and F. J. Navarro (2009a), On the effects of divide migration, along-ridge flow, and basal sliding on isochrones near an ice divide, *J. Geophys. Res.*, *114*, F02006, doi:10.1029/2008JF001025.
- Martin, C., G. H. Gudmundsson, H. D. Pritchard, and O. Gagliardini (2009b), On the effects of anisotropic rheology on ice flow, internal structure, and the age-depth relationship at ice divides, *J. Geophys. Res.*, *114*, F04001, doi:10.1029/2008JF001204.
- Martin, C., G. H. Gudmundsson, and E. C. King (2014), Modelling of Kealey Ice Rise, Antarctica, reveals stable ice-flow conditions in East Ellsworth Land over millennia, *J. Glaciol.*, *60*(219), 139–146, doi:10.3189/2014JoG13J089.
- Martin, P., and T. Sanderson (1980), Morphology and dynamics of ice rises, *J. Glaciol.*, *25*(91), 33–45.
- Matsuoka, K., F. Pattyn, D. Callens, and H. Conway (2012), Radar characterization of the basal interface across the grounding zone of an ice-rise promontory in East Antarctica, *Ann. Glaciol.*, *53*(60), 29–34, doi:10.3189/2012AoG60A106.
- Nereson, N., and C. Raymond (2001), The elevation history of ice streams and the spatial accumulation pattern along the Siple Coast of West Antarctica inferred from ground-based radar data from three inter-ice-stream ridges, *J. Glaciol.*, *47*(157), 303–313, doi:10.3189/172756501781832197.
- Nereson, N., C. Raymond, R. Jacobel, and E. Waddington (2000), The accumulation pattern across Siple Dome, West Antarctica, inferred from radar-detected internal layers, *J. Glaciol.*, *46*(152), 75–87, doi:10.3189/172756500781833449.
- Nereson, N. A., and E. D. Waddington (2002), Isochrones and isotherms beneath migrating ice divides, *J. Glaciol.*, *48*(160), 95–108, doi:10.3189/172756502781831647.
- Nereson, N. A., C. F. Raymond, E. D. Waddington, and R. W. Jacobel (1998), Migration of the Siple Dome ice divide, West Antarctica, *J. Glaciol.*, *44*(148), 643–652.
- Pattyn, F., S. De Brabander, and A. Huyghe (2005), Basal and thermal control mechanisms of the Ragnhild glaciers, East Antarctica, *Ann. Glaciol.*, *40*(1), 225–231, doi:10.3189/172756405781813672.
- Pettit, E., E. Waddington, W. Harrison, T. Thorsteinsson, D. Elsberg, J. Morack, and M. Zumbege (2011), The crossover stress, anisotropy and the ice flow law at Siple Dome, West Antarctica, *J. Glaciol.*, *57*(201), 39–52.
- Pettit, E. C., and E. D. Waddington (2003), Ice flow at low deviatoric stress, *J. Glaciol.*, *49*(166), 359–369, doi:10.3189/172756503781830584.
- Pettit, E. C., H. P. Jacobson, and E. D. Waddington (2003), Effects of basal sliding on isochrones and flow near an ice divide, *Ann. Glaciol.*, *37*, 370–376, doi:10.3189/172756403781815997.
- Pettit, E. C., T. Thorsteinsson, H. P. Jacobsen, and E. D. Waddington (2007), The role of crystal fabric in flow near an ice divide, *J. Glaciol.*, *53*(181), 277–288, doi:10.3189/172756507782202766.
- Pimienta, P., P. Duval, and V. Y. Lipenkov (1987), Mechanical behavior of anisotropic polar ice, in *Symposium on the Physical Basis of Ice Sheet Modelling, Publication 170*, edited by E. D. Waddington, and J. S. Walder, pp. 57–66, Int. Assoc. of Hydrol. Sci., Vancouver, Canada.
- Pollard, D., and R. M. DeConto (2009), Modelling West Antarctic ice sheet growth and collapse through the past five million years, *Nature*, *458*(7236), 329–332, doi:10.1038/nature07809.
- Purucker, M. (2013), Geothermal heat flux data set based on low resolution observations collected by the CHAMP satellite between 2000 and 2010, and produced from the MF-6 model following the technique described in Fox Maule et al. (2005). [Available at <http://websrv.cs.umd.edu/isis/index.php>, last access 23 March.]
- Raymond, C. F. (1983), Deformation in the vicinity of ice divides, *J. Glaciol.*, *29*(103), 357–373.
- Rignot, E., J. Mouginot, and B. Scheuchl (2011), Ice flow of the Antarctic ice sheet, *Science*, *333*(6048), 1427–1430.
- Schött-Hvidberg, C. (1996), Steady-state thermomechanical modelling of ice flow near the centre of large ice sheets with the finite-element technique, *Ann. Glaciol.*, *23*, 116–123.
- Vaughan, D. G., H. F. J. Corr, C. S. M. Doake, and E. D. Waddington (1999), Distortion of isochronous layers in ice revealed by ground-penetrating radar, *Nature*, *398*(6725), 323–326, doi:10.1038/18653.
- Waddington, E. D., J. F. Bolzan, and R. B. Alley (2001), Potential for stratigraphic folding near ice-sheet centers, *J. Glaciol.*, *47*(159), 639–648, doi:10.3189/172756501781831756.
- Waddington, E. D., T. A. Neumann, M. R. Koutnik, H.-P. Marshall, and D. L. Morse (2007), Inference of accumulation-rate patterns from deep layers in glaciers and ice sheets, *J. Glaciol.*, *53*(183), 694–712, doi:10.3189/002214307784409351.

- Wesche, C., S. Riedel, and D. Steinhage (2009), Precise surface topography of the grounded ice ridges at the Ekströmisen, Antarctica, based on several geophysical data sets, *ISPRS J. Photogramm. Remote Sens.*, *64*(4), 381–386, doi:10.1016/j.isprsjprs.2009.01.005.
- Whitehouse, P. L., M. J. Bentley, and A. M. L. Brocq (2012), A deglacial model for Antarctica: Geological constraints and glaciological modelling as a basis for a new model of Antarctic glacial isostatic adjustment, *Quat. Sci. Rev.*, *32*, 1–24, doi:10.1016/j.quascirev.2011.11.016.
- Yamane, M., Y. Yokoyama, H. Miura, H. Maemoku, S. Iwasaki, and H. Matsuzaki (2011), The last deglacial history of Lützow-Holm Bay, East Antarctica, *J. Quat. Sci.*, *26*(1), 3–6, doi:10.1002/jqs.1465.